# Beating the Rayleigh limit: Orbital-angular-momentum-based super-resolution diffraction tomography

Lianlin Li[1] and Fang Li[2]
[1]*Center of Advanced Electromagnetic Imaging, Department of Electronics, Peking University, Beijing 100871, China*
[2]*Institute of Electronics, CAS, Beijing 100190, China*
(Received 19 June 2013; revised manuscript received 13 August 2013; published 30 September 2013)

This paper reports a super-resolution imaging approach based on orbital-angular-momentum diffraction tomography (OAM-DT), which makes an important breakthrough on the Rayleigh limit associated with conventional diffraction tomography (DT) technique. It is well accepted that orbital-angular momentum (OAM) provides additional electromagnetic degrees of freedom. This concept has been widely applied in science and technology. In this paper we revisit the DT problem extended with OAM, and demonstrate theoretically and numerically that there is no physical limit on imaging resolution with OAM-DT. The physical mechanism behind it is that either the near field or superoscillation of the transmitter is employed to super-resolve probed objects. This super-resolution OAM-DT imaging paradigm does not require near-field measurement, a subtle focusing lens, or complicated postprocessing, etc., thus providing an approach to realize the wave-field imaging of universal objects with subwavelength resolution.

DOI: 10.1103/PhysRevE.88.033205 PACS number(s): 41.20.Jb, 42.30.Wb, 02.30.Zz, 07.05.Pj

## I. INTRODUCTION

In 1879 Lord Rayleigh formulated a criterion that a conventional imaging system cannot achieve a resolution beyond that of the diffraction limit, i.e., the Rayleigh limit. Such a "physical barrier" characterizes the minimum separation of two adjacent objects that an imaging system can resolve. In the past decade numerous efforts have been made to achieve imaging resolution beyond the Rayleigh limit. Among various proposals dedicated to surpassing this "barrier," a representative example is the well-known technique of near-field imaging, an essential subwavelength imaging technology. Near-field imaging relies on the fact that the evanescent component carries fine details of the electromagnetic field distribution at the immediate vicinity of probed objects [1]. Over the past decades, several innovative imaging instruments (e.g., the metamaterial superlens [2], metalens [3], etc.) have been invented, which detect the evanescent spectrum well to improve imaging resolution and operational distance of sensors to certain extents. Nonetheless, the strong confinement of measurements for near-field evanescent components precludes their widespread use as tools for general-purpose applications. To circumvent this limitation, superoscillation-based imaging has been developed as an alternative attempt to break the Rayleigh limit [4]. The superoscillatory method indicates that over a *finite* interval, a wave form oscillates arbitrarily faster than its highest component in its operational spectrum, and thus makes it possible to encode fine details of the probed object into the field of view beyond the evanescent fields. In light of this property, several optics devices have been built to achieve super-resolution imaging from far-field measurements [4,5]. Although superoscillation-based imaging alleviates the requirement of probe-object proximity, the achievable enhancement in resolution is essentially dependent on signal-to-noise ratio (SNR) and other factors, and it requires a huge-size mask with enough fabrication finesse. In addition to the methods mentioned above, there are other approaches that try to beat the Rayleigh limit; for example, most recently Gazit *et al*. proposed a technique of computational imaging which is dedicated for sparse or compressible objects via solving a time-consuming nonlinear optimization problem constrained by sparse regularization [6].

It is well known that the electromagnetic fields can carry not only energy and linear momentum but also angular momentum [decomposed into spin-angular momentum (SAM) and orbital-angular momentum (OAM)] over a very large distance [7]. It has been demonstrated that in the optics [8] and radio regimes [9], a beam with the distribution of a helical phase front carries the OAM information. Several solutions to generate this kind of vortex field have been developed as well [9,17]. OAM-carrying beams can provide more fruitful degrees of freedom for beam manipulation, and has been benefiting applications ranging from information processing and communications [10,11] to imaging in the optical and quantum regimes [12]. However, less than ten years ago researchers realized that OAM is promising for resolving two optical sources separated at a distance smaller than that of the Rayleigh limit. Swartzlander discovered that the optical vortex mask with unit topological charge can be applied to distinguish two sources separated by a distance slightly smaller than that of the Rayleigh criterion [13]. Tamburini *et al*. found out that when two sources separated by an angular distance below the Rayleigh criterion crossed an optical vortex mask with unit topological charge, the peak intensity ratio was highly sensitive to the distance between the separated sources; hence it can be used as a means to resolve two sources spaced at a distance smaller than the Rayleigh limit [14]. These methods aiming to break the Rayleigh limit seek to build heuristically the relation between the measured OAM spectrum and some critical parameters of targets of interests, such as location, size, and number of separated objects [15,16]. In this paper, we revisit the problem of diffraction tomography (DT) and formulate a variant by exploiting the concept of OAM, termed OAM-DT. The core idea behind the OAM-DT is that either the near field or superoscillation of the transmitter is employed to super-resolve probed objects. The current study indicates that this technology has no physical limits on imaging resolution

 

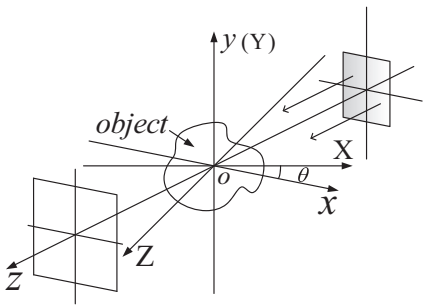


FIG. 1. The geometrical configuration adopted to study OAM-DT.

in principle, and can be universally used for imaging of complicated objects.

## II. PROPOSED METHODOLOGY

Diffraction tomography is capable of not only retrieving quantitatively the distribution of the dielectric constant of weak scattering objects, but also treating strong ones [18,19]. To facilitate discussion, we adopt the configuration of transmission measurement, as sketched in Fig. 1. In this setup, there are two sets of coordinate systems; namely, the local system $O$-$xyz$ is obtained by rotating the global system of $O$-$XYZ$ around the $y$ axis by $\theta$. The transmitter array is distributed within the region denoted by a gray-filled square located at $z_t$ while the array of receivers is at $z_r$. According to the vectorial wave equation, a time-harmonic electrical field $\mathbf{E}(\mathbf{r},\omega)$, in the inhomogeneous nondispersive medium with relative dielectric parameter $\varepsilon(\mathbf{r})$, obeys [21]

$$\nabla^2\mathbf{E}(\mathbf{r},\omega)+k_0^2\varepsilon(\mathbf{r})\mathbf{E}(\mathbf{r},\omega)+\nabla[\mathbf{E}(\mathbf{r},\omega)\cdot\nabla\ln\varepsilon(\mathbf{r})]=0, \quad (1)$$

where $k_0=2\pi/\lambda$ is the wave number in free space, and $\lambda$ is the operating wavelength. With the assumption of slowly varying medium in the scale of $\lambda$, i.e., $|\nabla\ln\varepsilon(\mathbf{r})|\ll\lambda$, the third term in the left-hand side of Eq. (1) falls off [21]; consequently,

$$\nabla^2\mathbf{E}(\mathbf{r},\omega)+k_0^2\varepsilon(\mathbf{r})\mathbf{E}(\mathbf{r},\omega)=0. \quad (2)$$

Here three components of $\mathbf{E}(\mathbf{r},\omega)$ are decoupled in Eq. (2). For convenience, the nonbold letter $E$ for a component of $\mathbf{E}$ is utilized below, and the argument $\omega$ is suppressed as well.

With the use of the Born approximation, the OAM-carrying electrical field $E_{\rm sca}(\mathbf{r},\ell)$ scattered from probed targets reads

$$E_{\rm sca}(\mathbf{r},\ell)=\int_{\rm ROI}G(\mathbf{r},\mathbf{r}')E_{\rm in}(\mathbf{r}',\ell)O_{\rm 3D}(\mathbf{r}')d\mathbf{r}',$$
$$\mathbf{r}=(x,y,z)\in D_r,\ \ \mathbf{r}'=(x',y',z')\in{\rm ROI}. \quad (3)$$

Herein, $D_r$ is the region where receivers are placed, $O_{\rm 3D}(\mathbf{r}')=k_0^2[\varepsilon(\mathbf{r})-1]$ represents the contrast of three-dimensional (3D) objects with respect to background medium (free space in this paper), $G(\mathbf{r},\mathbf{r}')=\frac{e^{jk_0|\mathbf{r}-\mathbf{r}'|}}{4\pi|\mathbf{r}-\mathbf{r}'|}$ is the Green's function in free space, and $j=\sqrt{-1}$. Inside the region of interest (ROI) where the probed objects are embedded, the incident wave is assumed to be OAM-carrying with the topological charge of $\ell$ ($\ell=0,\pm1,\pm2,\ldots,\pm L$), and propagates along the $z$ direction, i.e., $E_{\rm in}(\mathbf{r}',\ell)=A(r')e^{j(\ell\varphi'+k_0z')}$, where $\varphi'$ is the polar angular in the $O$-$xy$ plane, and the core of this vortex field is along the $z$ axis. In this work $E_{\rm in}(\mathbf{r}',\ell)=e^{j(\ell\varphi'+k_0z')}$ is adopted. Bear in mind that the case of $\ell=0$ corresponds to traditional DT technique.

Following the line adopted in the standard DT technique, the algorithm implementation of OAM-DT super-resolution imaging can be straightforwardly developed. In the matrix form, Eq. (1) becomes

$$\mathbf{E}_\ell=\mathbf{A}_\ell O_{\rm 3D}, \quad (4)$$

where $\ell=0,\pm1,\pm2,\ldots,\pm L$; $L$ is a truncated number. Equation (4) can be immediately solved by a standard least squares method; more specifically, the solution reads

$$\hat{\mathbf{O}}_{\rm 3D}=\left[\sum_{\ell=-L}^{L}\mathbf{A}_\ell^*\mathbf{A}_\ell\right]^{-1}\left[\sum_{\ell=-L}^{L}\mathbf{A}_\ell^*\mathbf{E}_\ell\right], \quad (5)$$

where the superscript $^*$ indicates the conjugate transpose.

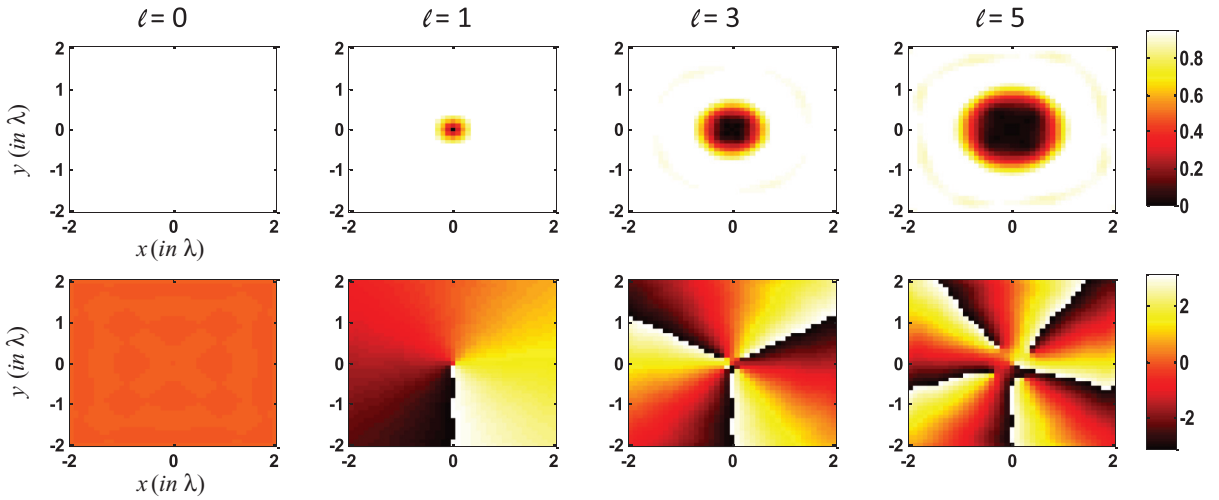


FIG. 2. (Color online) The distributions of normalized amplitudes (top row) and phases (bottom row) of OAM-carrying fields at $z=0$ produced by the phased antenna array located at $z_t=-5\lambda$. From left to right, they correspond to $\ell=0$, 1, 3, and 5. In these figures, all axes are scaled by operational wavelength $\lambda$.

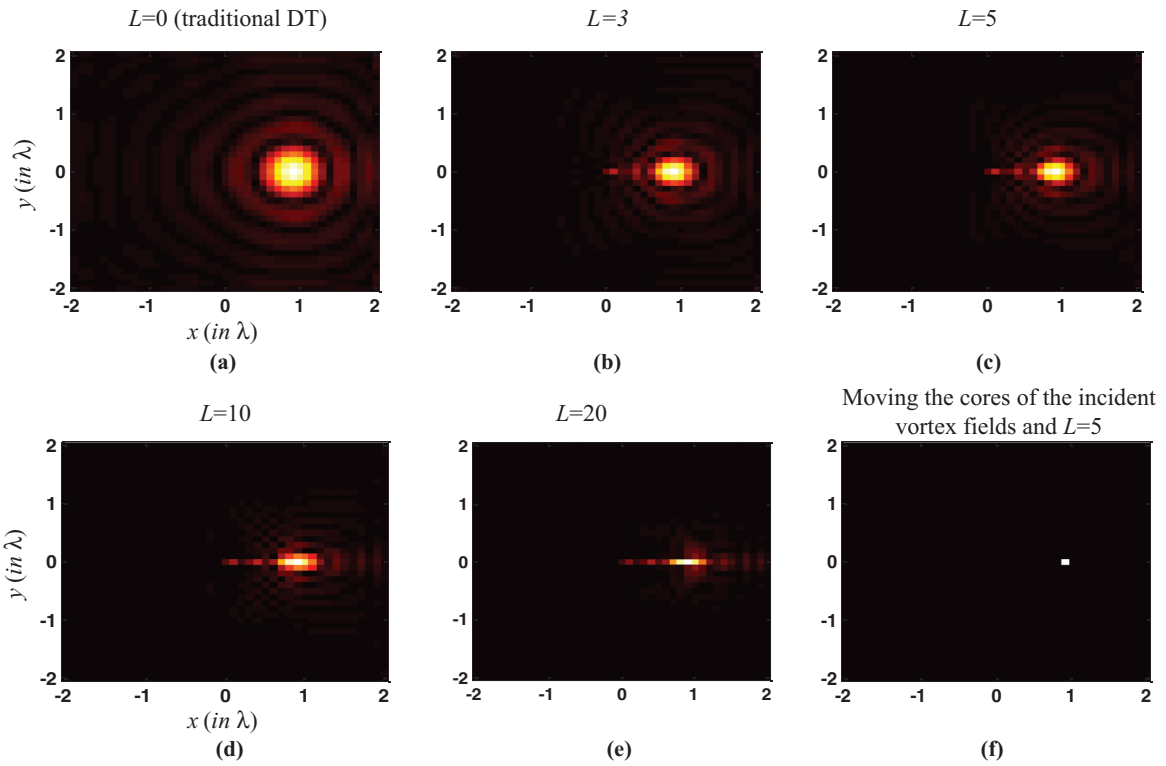


FIG. 3. (Color online) Reconstruction of a small cube with a size of $0.1\lambda \times 0.1\lambda \times 0.1\lambda$, and refraction index of 1.01. (a) $L = 0$ (equivalent to traditional DT method), (b) $L = 3$, (c) $L = 5$, (d) $L = 10$, and (e) $L = 20$. From (a) to (e), the cores of the incident vortex fields are located at the origin of the global coordinate system. Panel (f) is the result of moving the cores of incident vortex fields along $x = \lambda$. In all of these images, all axes are scaled by operational wavelength $\lambda$.

### A. The generation of OAM-carrying illumination

In optics, there are numerous methods of generating OAM-carrying beams, such as with the use of a spiral phase plate (SPP), computer-aided hologram, etc. In radio, it was shown that an OAM-carrying radio beam can be generated by a circular phased antenna array [9], or other means [17]. In this paper the OAM-carrying field of $E_{\text{in}}(r') = A(r')e^{j(\ell\varphi'+k_0z')}$ inside the ROI is produced by a phase antenna array. In the simulation 400 elements of half-wavelength dipoles are uniformly distributed within the rectangle plane of $[-5\lambda, 5\lambda] \times [-5\lambda, 5\lambda]$ at $z_t = -5\lambda$. OAM-carrying radio beams can be generated by adaptively controlling phases and amplitudes of elements of the antenna array. In the top row of Fig. 2, the distributions of normalized amplitudes of resulting incident fields inside at the location of $z = 0$ are illustrated for topological charges of $\ell = 0$, 1, 3, and 5 from left to right. In the bottom row of Fig. 2, corresponding phase distributions are shown as well. Notice that the sizes of the vortex fields follow the rules, in particular, (a) $E_{\text{in}}(r',\ell) \approx e^{j\ell\varphi'}$ for $r' \geqslant r_0(\ell)$, otherwise being approximately zero, where $r_0(\ell)$ is a positive nondecreasing function of $|\ell|$; for instance, $r_0(\ell) \approx 0.16|\ell|$ for $z_t = -5\lambda$. (b) For a given value of $\ell$, $r_0(\ell)$ is inversely proportional to the distance $|z_t|$.

### B. Super-resolution imaging mechanism

We investigate the capability of the OAM-DT scheme for super-resolution imaging by examining the imaging of a thin dielectric slab, mathematically, $O_{3D}(\mathbf{r}') = O(x',y')\delta(z')$. For this case only one-view measurements are taken into consideration, specifically, $\theta = 0$. Regarding the reconstruction of more general 3D objects, discussions in this article are applicable with multiview measurements by changing $\theta$. After applying the Weyl equation [21] to the Green's function in Eq. (1), we obtain

$$E_{\text{sca}}(x,y,\ell) = \frac{j}{8\pi^2}\int_{-\infty}^{+\infty}\int_{-\infty}^{+\infty} dk_x dk_y \times \tilde{O}(k_x,k_y;\ell)\frac{e^{jk_xx+jk_yy-jk_zz_r}}{k_z}, \quad (6)$$

where $k_z = \sqrt{k_0^2 - k_x^2 - k_y^2}$, $\tilde{O}_\ell(k_x,k_y) = \int O(x',y')e^{j\ell\varphi'}e^{-jk_xx'-jk_yy'}dx'dy'$. Taking the two-dimensional (2D) Fourier transform of $E_{\text{sca}}(x,y,\ell)$ with respect to $x$ and $y$ leads to

$$\tilde{E}_{\text{sca}}(k_x,k_y,\ell) \propto \frac{e^{jk_zz_r}}{k_z}(\tilde{O} \otimes \tilde{F}_\ell)(k_x,k_y), \quad (7)$$

where $\otimes$ indicates convolution, $\tilde{O}(k_x,k_y) = \int O(x',y')e^{-jk_xx'-jk_yy'}dx'dy'$, and [22]

$$\tilde{F}_\ell(k_x,k_y) = \int e^{-jk_xx'-jk_yy'}e^{j\ell\varphi'}r'dr'd\varphi' \propto j^{-|\ell|}e^{j\ell\theta_k}\int_0^\infty J_{|\ell|}(kr')r'dr' \propto j^{-|\ell|}|\ell|k^{-2}e^{j\ell\theta_k}. \quad (8)$$

Here $\theta_k = \tan^{-1}(k_y/k_x)$, and $J_{|\ell|}(\cdot)$ is the $|\ell|$-order first-kind Bessel function. It is not hard to prove that in the far field of

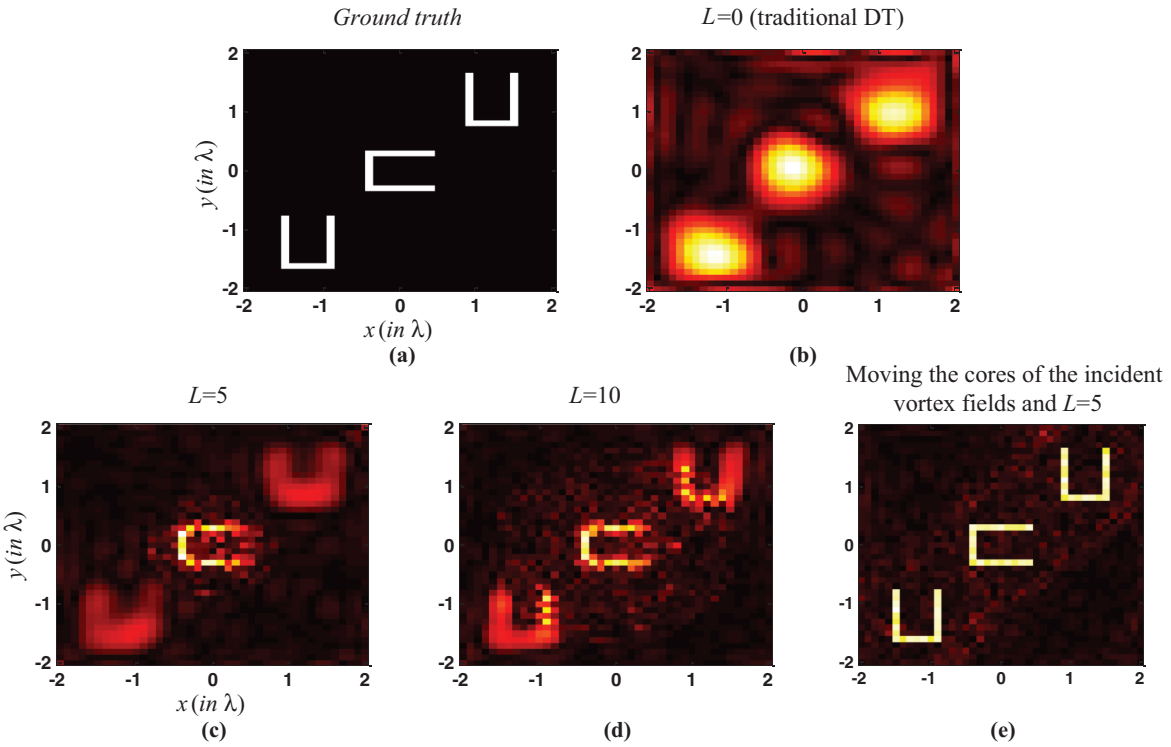


FIG. 4. (Color online) (a) The ground truth. (b) The result obtained by traditional DT method. (c), (d) The results of OAM-DT with $L = 5$ and $L = 10$, respectively. (e) The result of moving the cores of incident vortex fields along the diagonal of ROI. For all these figures, all axes are scaled by working wavelength λ.

$k_0 z_r \gg 1$ and $\ell = 0$, $\tilde{E}_{\rm sca}(k_x,k_y,\ell) \propto \frac{e^{-jk_z z_r}}{k_z}\tilde{O}(k_x,k_y)$ is band limited to $k_x^2 + k_y^2 \leqslant k_0^2$ which attributes to the Rayleigh limit. In contrast, the convolution depicted in Eq. (4) with nonzero $\ell$ allows the conversion of high-frequency components of $\tilde{O}(k_x,k_y)$ outside $k_x^2 + k_y^2 \leqslant k_0^2$ into $\tilde{E}_{\rm sca}(k_x,k_y,\ell)$ inside $k_x^2 + k_y^2 \leqslant k_0^2$, giving rise to the feasibility of super-resolution imaging. It can be shown clearly by applying $\sum_{\ell=-\infty}^{\infty} e^{j\ell(\varphi-\varphi')} = \delta(\varphi - \varphi')$ to Eq. (7), that the deduced imaging with arbitrarily high angular resolution, at least in principle, can be readily achieved.

In the following, further insights into the super-resolution imaging mechanism by OAM-DT are discussed from two aspects, i.e., near-field coupling and superoscillation. Firstly, Eq. (2) exhibits that there is a spatial-frequency mixing characterized by the multiplication between illumination $E_{\rm in}(\mathbf{r}',\ell)$ and probed target $O_{\rm 3D}(\mathbf{r}')$. That is when the illumination contains a spatial frequency $\mathbf{k}_{\rm in}$; then spatial frequency $\mathbf{k}$ of the probed target can be observable if it lies within the region of $|\mathbf{k}_{\rm in} - \mathbf{k}| \leqslant k_0$, where the far-field observation, i.e., large $|z_r|$, is implied. Consequently, to maximize the resolution it is desirable for the illumination to contain as high spatial frequency $\mathbf{k}_{\rm in}$ as possible. On the other hand, the $E_{\rm in}(\mathbf{r}',\ell)$, generated by a array of phased antennas located at $z_t$, is formally expressed by

$$E_{\rm in}(\mathbf{r}',\ell) = \sum_m \sum_n J_{m,n} G\left(\mathbf{r}',\mathbf{r}_{m,n}\right). \tag{9}$$

Here, $J_{m,n}$ is the exciting complex-valued current of the $(m,n)$th antenna element. In the case of a small $|z_t|$, i.e., *the probed target is placed closely to the array of transmitting antennas*, the module of $\mathbf{k}_{\rm in}$ can be substantially larger than $k_0$ owing to evanescent wave components of fields from transmitting antennas. As a result, the super-resolved imaging can be readily deduced from far-field measurements, i.e., $k_0|z_r| \gg 1$.

Secondly, the OAM-based super-resolved imaging can be obtained for the large $|z_t|$ from so-called superoscillation phenomena. Superoscillation means that a band-limited function can be oscillating arbitrarily faster than its highest Fourier component within a finite interval. It is the fact that the spatial bandwidth of the whole illumination radiated from transmitters cannot be beyond $k_0$, which means that an incident wave cannot be characterized by $e^{j\ell\varphi'}$ in the whole space. However, it can be faithfully conceived that the illumination can be well approximated to be of $e^{j\ell\varphi'}$ within a region of $r_1 \leqslant r' < r_2$ ($r_1$ and $r_2$ are two non-negative real numbers). Thus, it is a clever way to place the probed targets inside the area of $r_1 \leqslant r' < r_2$; correspondingly, the integrand of Eq. (1), originally restricted into the domain of $r_1 \leqslant r' < r_2$, can be extended into the whole space, and Eq. (1) becomes

$$E_{\rm sca}(\mathbf{r},\ell) = \int G(\mathbf{r},\mathbf{r}') e^{j\ell\varphi'} O_{\rm 3D}(\mathbf{r}') d\mathbf{r}'. \tag{10}$$

Obviously, the "illumination" represented by $e^{j\ell\varphi'}$ contains a spatial frequency $\mathbf{k}_{\rm in}$ substantially higher than $k_0$, which immediately leads to the super-resolution imaging by the mixing-frequency principle as discussed above.

Finally, we would like to look into the above claim by considering the so-called point-spread function (PSF) of OAM-DT. After some straightforward implementation, the

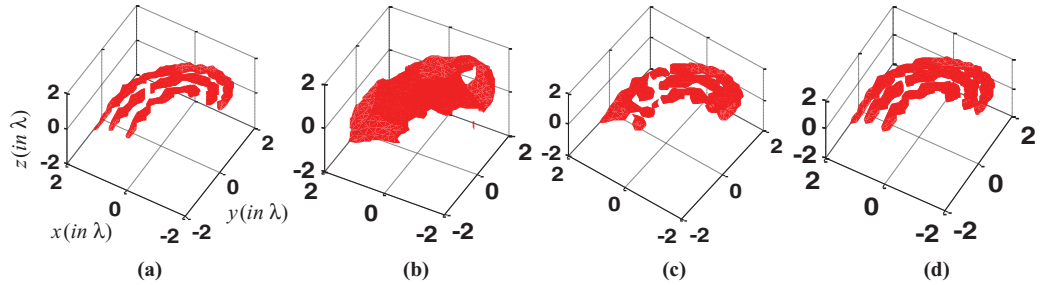


FIG. 5. (Color online) (a) The ground truth. (b) The result obtained by traditional DT method. (c) The result of OAM-DT with $L = 5$, where cores of incident vortex fields are fixed at the center of ROI. (d) The result of moving the cores of incident vortex fields along the diagonal of ROI. In these figures, all axes are scaled by working wavelength λ.

expression of the reconstruction of $O(x',y')$ in terms of PSF is

$$\hat{O}(x'',y'') = \int R(x',y';x'',y'')O(x',y')dx'dy',$$
$$(x',y'),(x'',y'') \in \text{ROI}, \tag{11}$$

where in the limit of $L \to \infty$ the PSF of OAM-DT is

$$\begin{aligned} R(x',y';x'',y'') &= \sum_{\ell=-\infty}^{\ell=+\infty} e^{-j\ell(\varphi'-\varphi'')} \int_{-\infty}^{+\infty}\int_{-\infty}^{+\infty} dk_x dk_y \\ &\quad \times \frac{e^{-2\text{Im}(k_z)z_r}}{|k_z|^2} e^{jk_x(x'-x'')+jk_y(y'-y'')} \\ &\approx \delta(\varphi'-\varphi'')\int_0^{k_0} J_0(k|r'-r''|)kdk \\ &= k_0\delta(\varphi'-\varphi'')\frac{J_1(k_0|r'-r''|)}{|r'-r''|}, \end{aligned} \tag{12}$$

where $\text{Im}(k_z)$ is the imagery part of $k_z$. Equation (12) reveals that with the use of topological charges varying from $-\infty$ to $\infty$, the extremely high angular resolution can be achieved while there is no obvious improvement in the radial resolution. Inspired by this we expect the imaging with super-resolution in the angular and radial directions can be obtained by changing cores of the vortex incident fields.

## III. RESULTS

To demonstrate previous investigations, a set of numerical experiments are conducted, where the synthetic measurements are generated using the full-wave simulation of method of moment (MoM) [20] and corrupted by some additive Gaussian noise. In the simulation the region of interest (ROI) of 4λ × 4λ × 0.1λ, centered at the origin, is divided into 41 × 41 × 1 sub-blocks with a size of 0.1λ × 0.1λ × 0.1λ, and only one-view measurements (i.e., $\theta = 0$) are served as the input of OAM-DT. An array of 30 × 30 receivers are arranged uniformly within a rectangle region of [–5λ, 5λ] × [–5λ, 5λ] at the location of $z = 5\lambda$, and distributed regularly within a square of 10λ × 10λ with a spatial step of 0.5λ. As the first example, the target being imaged consists of a small cube with a size of 0.1λ × 0.1λ × 0.1λ with a refraction index of 1.01 located at (0, λ, 0), and the SNR of the measurement is set to be 40 dB. Figure 3 compares reconstruction results obtained by traditional DT and the proposed OAM-DT technique. Figure 3(a) gives the result by traditional DT method equivalent to the case of $L = 0$, while Figs. 3(b)–3(e) are results by proposed OAM-DT with $L = 3$, 5, 10, and 20. These results reveal that with the increase of truncation index $L$, reconstructed images become remarkably sharper, especially the strong enhancement on the angular resolution, as predicted previously. To further improve the radial resolution, we move the cores of OAM-carrying incident fields from −1.5λ to 1.5λ with a step of 0.5λ along the line of $x = \lambda$, and the corresponding result is shown in Fig. 3(f), where the image is almost a perfect reconstruction of the "true" object. The second example is more complicated targets consisting of three separated U-shaped structures with different orientations. In this simulation, all parameters are the same as above except for a lower SNR of 30 dB. Figures 4(b)–4(d) give, respectively, the results reconstructed by OAM-DT techniques with $L = 0$ (traditional DT), 5, and 10. To improve imaging quality further, cores of OAM-carrying incident fields are moved along the diagonal of the ROI with steps of 0.5λ, and we use $L = 5$. The corresponding results demonstrated in Fig. 4(e) reveal an almost perfect reconstruction of the ground truth in Fig. 4(a).

In the last example, we consider the reconstruction of 3D objects [as shown in Fig. 5(a)] by applying the proposed OAM-DT approach, where the simulation data are produced by commercial software FEKO Suite 5.3 and are corrupted with white noise with SNR of 30 dB. In this case all other parameters are the same as the above examples. The simulation took multiview measurements of $\theta$ =0°, 45°, 90°, and 135°. Figure 5(c) shows the result of OAM-DT with $L = 5$. The corresponding results computed by standard DT technique are displayed in Fig. 5(b) for comparison. To further improve imaging quality, the centers of the vortex fields are moved along the diagonal of the ROI with step of 0.5, and the imaging results are shown in Fig. 5(d). A function of "*isosurface*" in MATLAB 7.3 with a threshold value of 0.0031 is applied in Figs. 5(c) and 5(d), while a value of 0.000 78 in Fig. 5(b) is due to relatively underestimated values by traditional DT technique. For this 3D example, conclusions drawn previously are confirmed.

## IV. CONCLUSION

In summary, in this paper we demonstrate theoretically and numerically that it is indeed possible to significantly refine the imaging resolution of traditional diffraction tomography by applying electromagnetic OAM. This discovery serves an approach for subwavelength wave-field imaging in a

rather efficient manner, which has no harsh requirements for elaborate imaging lens, near-field measurement, sophisticated and heavily computational postprocessing, etc. It is conceivable that the proposed OAM-DT technique is promising for the development of novel information-rich radar, smart antenna arrays, and other imaging systems. A concept-of-proof imaging system is under construction, and will be reported in the near future.


[1] J. Y. Lee, B. H. Hong, W. Y. Kim, S. K. Min, Y. Kim, M. V. Jouravlev, R. Bose, K. S. Kim, I.-C. Hwang, L. J. Kaufman, C. W. Wong, P. Kim, and K. S. Kim, Nature **460**, 498 (2009).

[2] J. B. Pendry, Phys. Rev. Lett. **85**, 3966 (2000).

[3] F. Lemoult, M. Fink, and G. Lerosey, Nat. Commun. **3**, 889 (2012).

[4] F. M. Huang and N. I. Zheludev, Nano Lett. **9**, 1249 (2009).

[5] E. T. F. Rogers, J. Lindberg, T. Roy, S. Savo, J. E. Chad, M. R. Dennis, and N. I. Zheludev, Nat. Mater. **11**, 432 (2012).

[6] S. Gazit, A. Szameit, Y. C. Eldar, and M. Segev, Opt. Express **17**, 23920 (2009).

[7] L. Allen, M. W. Beijersbergen, R. J. C. Spreeuw, and J. P. Woerdman, Phys. Rev. A **45**, 8185 (1992).

[8] G. Gibson, J. Courtial, M. J. Padgett, M. Vasnetsov, V. Pas'ko, S. M. Barnett, and S. Franke-Arnold, Opt. Express **12**, 5448 (2004).

[9] S. M. Mohammadi, L. K. S. Daldorff, J. E. S. Bergman, R. L. Karlsson, B. Thidé, K. Forozesh, T. D. Carozzi, and B. Rsham, IEEE Trans. Antennas Propag. **58**, 565 (2010).

[10] F. Tamburini, E. Mari, A. Sponselli, B. Thidé, A. Bianchini, and F. Romanato, New J. Phys. **14**, 033001 (2012).

[11] J. Wang, J.-Y. Yang, I. M. Fazal, N. Ahmed, Y. Yan, H. Huang, Y. Ren, Y. Yue, S. Dolinar, M. Tur, and A. E. Willner, Nat. Photonics **6**, 488 (2012).

[12] S. Furhapter, A. Jesacher, S. Bernet, and M. Ritsch-Marte, Opt. Express **13**, 689 (2005).

[13] G. A. Swartzlander, J. Opt. A: Pure Appl. Opt. **11**, 094022 (2009).

[14] F. Tamburini, G. Anzolin, G. Umbriaco, A. Bianchini, and C. Barbieri, Phys. Rev. Lett. **97**, 163903 (2006).

[15] T. Brunet, J.-L. Thomas, and R. Marchiano, Phys. Rev. Lett. **105**, 034301 (2010).

[16] L. Torner, J. P. Torres, and S. Carrasco, Opt. Express **13**, 873 (2005).

[17] D. Zelenchuk and V. Fusco, IEEE Antenna Wireless Propag. Lett. **12**, 284 (2013).

[18] A. J. Devaney, IEEE Trans. Geosci. Remote Sensing **GE-22**, 3 (1984).

[19] A. Schatzberg and A. J. Devaney, Inverse Probl. **8**, 149 (1992).

[20] Q. H. Liu, Z. Q. Zhang, and X. M. Xu, IEEE Trans. Geosci. Remote Sensing **39**, 347 (2001).

[21] M. Born and E. Wolf, *Principles of Optics,* 7th ed. (Cambridge University Press, Cambridge, 1999).

[22] M. V. Berry, J. Opt. A: Pure Appl. Opt. **6**, 259 (2004).